https://doi.org/10.1016/j.scriptamat.2015.12.031
This is the Pre-Published Version.

# Ultra Rapid Fabrication of p-type Li-doped $Mg_2Si_{0.4}Sn_{0.6}$ synthesized by unique melt spinning method

Xiaodan Tang[a,b], Guiwen Wang[a], Yong Zheng[a], Yumeng Zhang[a], Kunling Peng[a,b], Lijie Guo[a], Shuxia Wang[a], Min Zeng[c,d], Jiyan Dai[c], Guoyu Wang[b,*], Xiaoyuan Zhou[a,*]

[a]College of Physics, Chongqing University, Chongqing 401331, People's Republic of China.

[b]Chongqing Institute of Green and Intelligent Technology, Chinese Academy of Sciences, Chongqing 400714, People's Republic of China.

[c]Department of Applied Physics, The Hong Kong Polytechnic University Kowloon, Hong Kong.

[d]Institute for Advanced Materials and Guangdong Provincial Key Laboratory of Quantum Engineering and Quantum Materials, South China Normal University, Guangzhou 510006, People's Republic of China.

## Abstract

In this work, we successfully synthesized *p*-type $Mg_{2(1-x)}Li_{2x}Si_{0.4}Sn_{0.6}$ (x = 0.00, 0.01, 0.03, 0.07, 0.09) samples using a home-made melt spinning system combined with spark plasma sintering. Compared with the samples prepared by a traditional method, the processing time is reduced from typically several days to less than one hour. It is found that the electrical conductivity rises rapidly with the increase of Li content owing to the enhanced carrier density, while the Seebeck coefficient decreases concomitantly to some extent. Meanwhile, Li doping dramatically reduces the thermal conductivity, leading to an enhanced figure of merit ZT~ 0.58 at 760 K.

**Keywords:** *p*-type $Mg_2(Si,Sn)$; Melt Spinning; Thermoelectric Properties.

The growing energy demand and environmental degradation have spurred research to seek sustainable energy conversion technologies which will allow for a transition away from fossil fuels as the dominate source of energy. One such avenue lies in the area of thermoelectric materials, which can generate electricity from waste heat and play an important role in global sustainable energy solution [1]. The thermoelectric efficiency of material is determined by a dimensionless figure of merit $ZT = S^2\sigma T/\kappa$, where S, σ, T and κ are the Seebeck coefficient, the electrical conductivity, the temperature in Kelvin and the thermal conductivity respectively [2-5]. The electrical property is represented by the

© 2015. This manuscript version is made available under the CC-BY-NC-ND 4.0 license https://creativecommons.org/licenses/by-nc-nd/4.0/.

power factor (PF=$S^2\sigma$). High ZT is desired for good thermoelectric performance by means of improving PF which is generally optimized by doping [6], and minimizing κ by usually enhancing scattering mechanisms [7].

Among the promising thermoelectric materials, the $Mg_2(Si,Sn)$-based compounds have received considerable attention as potential high-performance thermoelectric materials since the 1950s due to their non-toxicity, environmental friendliness, the abundance of their constituent elements in the earth's crust [8-10]. Attempts have been made to improve the figure of merit of $Mg_2(Si,Sn)$-based materials through the addition of dopants [11], point defect chemistry approach [12], and introducing different phonons scattering mechanisms [13-14]. To date, the maximum ZT achieved in *n*-type $Mg_2(Si,Sn)$-based compounds is~1.55 for Bi-doped $Mg_2Si_{0.4}Sn_{0.6}$ [15]. However, the ZT values for *p*-type $Mg_2(Si,Sn)$-based materials mostly remain below unity. As we all know, both n-type and p-type legs are needed for power generation devices to maximize power output for practical application. Thus, it is extremely urgent to enhance the thermoelectric performance of p-type $Mg_2(Si,Sn)$-based materials considering their poor thermoelectric performance. Recently, H.Ihou-Mouko*et al*. synthesized Ga filled *p*-type $Mg_2(Si,Sn)$-based compounds and reported a peak ZT of 0.36 at 625 K in $Mg_2Si_{0.6}Ge_{0.4}$:Ga(0.8%) [16]. Y. Isoda *et al*. synthesized Ag/Li double-filled *p*-type $Mg_2(Si,Sn)$-based compounds and reported a peak ZT of 0.32 at 610 K in $Mg_2Si_{0.25}Sn_{0.75}$ with Li-5000 ppm and Ag-20000 ppm [17].X. F. Tang *et al*. synthesized Li filled *p*-type $Mg_2(Si,Sn)$-based compounds and reported a peak ZT of 0.5 at 750 K in $Mg_{1.86}Li_{0.14}Si_{0.3}Sn_{0.7}$ [18].

Current strategies to prepare $Mg_2(Si,Sn)$-based sample are multitudinous, such as two-step solid-state reaction [19], modified bridgeman method [20], induction melting [21], and melt spinning [22] et al. Among them, melt spinning (MS) is a novel approach used for the rapid fabrication of conventional thermoelectric. Due to the ultra-high cooling rate in the melt-spinning process, notably refined grains can be obtained, resulting in a great reduction of the lattice thermal conductivity in comparison with materials prepared by the traditional method. Besides, in contrast to solid state reaction method, the preparation time can be significantly shortened via the melt spinning method, namely, shorten from ~10

days to less than one day. Another advantage for melt spinning is the homogeneous structure in the final product, which could enhance carrier mobility and electrical conductivity. X. F. Tang *et al*. at Wuhan University of Technology conducted some pioneering work on n-type $Mg_2(Si,Sn)$ based compounds by melt-spinning combined with plasma activated-sintering (PAS). A high figure of merit ZT ~1.3 at 750 K is obtained in n-type Sb-doped $Mg_2Si_{0.3}Sn_{0.7}$, a 15% improvement over the traditional solid states reaction samples [22]. However, an ingot previously made by solid states reaction is required for the subsequent melt spinning processing in their study, complicating the whole processing and extending the synthesis cycle. As driven by the market, further reduction of the fabrication time and cost is imperative. In addition, due to the fact that Mg is easily oxidized in air, to prevent any contamination of oxygen is vital to assure the quality of the final product. Unfortunately, the existing melt spinning method of $Mg_2(Si,Sn)$-based materials is very difficult to achieve this point. In our work, we employed a home-made melt spinning system assembled inside the glove box to prepare $Mg_{2(1-x)}Li_{2x}Si_{0.4}Sn_{0.6}$ (x = 0.00, 0.01, 0.03, 0.07, 0.09) compounds and successfully avoided the production of MgO. A figure of merit ZT up to ~0.58 is achieved at 760K when x is equal 0.07, an improvement by 15% as compared to the record value to date.

High-purity bulk of Mg (99.5%), Sn (99.9%), Li (99.9%), and powder of Si (99.99%) were weighed according to the stoichiometry $Mg_{2(1-x)}Li_{2x}Si_{0.4}Sn_{0.6}$ (x = 0.00, 0.01, 0.03, 0.07, 0.09), with a 5at% excess of Mg to compensate for the evaporation loss of Mg element during melt spinning (MS). All these raw materials were molten under 1133-1173 K for 10 min in a graphite tube and then injected under a pressure of 0.07 MPa Ar onto the edge of a chilled copper roller with a rotating speed of 25 m/s, and rapidly solidified into the thin ribbons. All the above operations were done inside an argon glove box to prevent any contamination of oxygen. The obtained ribbons were subsequently collected and pulverized in an agate mortar, then compacted by using Spark Plasma Sintering (SPS) at 873 K for 5 min under the pressure of 40 MPa. The final products possess density greater than 95% of the theoretical density, and the obtained cylinders were subsequently cut into different bulk with appropriate size and shape for electrical and thermal transport

properties measurements. The Seebeck coefficient $S$ and electrical conductivity $\sigma$ were measured on the rectangular-shaped samples with a commercial system (LSR-3, Linseis) under the protective atmosphere of Helium. The thermal conductivity $k$ was calculated by the equation of $k = \lambda\rho C_P$ , where $\lambda$ is the thermal diffusivity, $\rho$ is the geometric density, and $C_p$ is the heat capacity. The $\lambda$ and $C_p$ were measured by the laser flash method (Netzsch, LFA 457) and scanning calorimeter (Netzsch, 404 F3), respectively. The densities d of samples were calculated from the sample dimensions and mass. The above mentioned thermoelectric properties of $S$, $\sigma$ and $k$ were measured from room temperature to 773 K. The carrier concentrations of all samples at room temperature were tested by a home-made Hall apparatus under a magnetic field of 1 T and carrier mobility $\mu$ was calculated according to the equation $\sigma=nq\mu$. The phase compositions of the samples were detected by powder X-ray diffractometer using the PANalytical X'pert Pro type apparatus with Cu $K_\alpha$ radiation. The polarized micro-Raman spectra between 100 and 500 $cm^{-1}$ were measured at room temperature with the Raman spectrometer (JY-HR800). The morphology and microstructure of our samples were investigated using the field emission scanning electron microscopy (JSM-7800F, JEOL) and the transmission electron microscopy (TEM, JEOL, 2100F).

Powder XRD patterns for these $Mg_{2(1-x)}Li_{2x}Si_{0.4}Sn_{0.6}$ (x = 0.00, 0.01, 0.03, 0.07, 0.09) ribbons and bulk after SPS are shown in Figures 1(a) and (b), respectively. It is apparent that all these samples show only the Bragg peaks associated with an anti-fluorite structure (space group, Fm3m) without presence of any impurity phase, indicating that single phase $Mg_{2(1-x)}Li_{2x}Si_{0.4}Sn_{0.6}$ compounds have been successfully synthesized via our homemade melt spinning system followed by SPS. Compared to the XRD pattern for $Mg_{2(1-x)}Li_{2x}Si_{0.4}Sn_{0.6}$ bulk as shown in Figure 1(b), one can see that quite wider and weaker peaks appear for ribbons after MS, as shown in Figure 1(a), owing to the microstructure refinement during the rapid-melt quenching process. In addition, as shown in both Figures 1(a) and 1(b), no peak shift can be observed as the Li content increases, indicating that the addition of several percent of Li does not change lattice parameters of $Mg_2(Si,Sn)$-based compounds. This in turn indicates the disappearance of the lattice strain built-up, which

might otherwise has a detrimental effect on the carrier mobility [23-24]. Raman spectra, as shown in Figure 1(c), were also obtained for $Mg_2(Si,Sn)$-based compounds. Only one peak can be seen in each sample and all the peaks are in the range of 227~234 $cm^{-1}$, indicating that the samples are pure and $Mg_2(Si,Sn)$-based solid solution have been successfully synthesized; the peak position of $Mg_2Si$ and $Mg_2Sn$ are located at 258$cm^{-1}$ and 220$cm^{-1}$ [25], respectively.

Figures 2(a) and 2(b) show the SEM images of the face in contact with the edge of the copper wheel and free face of the ribbon, respectively. The microstructure of fractured surfaces of our bulk after SPS is shown in Figures 2(c). As indicated in Figures 2(a) and 2(b), the contact face of the ribbon is smoother than the free face. There exists little grain structure on the contact surface of the ribbon, while much nano- and microscaled grains can be found on the free face of the ribbon. These differences in microstructures are mainly due to the difference in cooling rates during the quenching process for two surfaces. As shown in Figure 2(c), the crystal grains are closely packaged together and no obvious holes can be found, being consistent with the high density of our bulk samples. Furthermore, the grain size is almost in the range of micrometer-scale, which is mainly attributed to grains growth during the SPS process, and there are no nanoscaled precipitates can be identified. To further verify the phase of $Mg_{2(1-x)}Li_{2x}Si_{0.4}Sn_{0.6}$ compounds, TEM images of the sample $Mg_{2(1-x)}Li_{2x}Si_{0.4}Sn_{0.6}$ with x=0.07 are shown in Figures 2(d) and 2(e). In Figure 2(d), numerous nanoscaled precipitates, similar to the published result [26-27], can be seen. Since the nanoprecipitates are overlapped with the matrix, it is difficult to get exact composition of the nanoprecipitates by energy dispersive x-ray (EDX) analysis. However, EDX analysis on the area with much darker-contrast nanoprecipitates reveals that the content of Sn is relatively higher than the matrix. Therefore, it is suspected that those nanoprecipitates are Sn-riched phase. This is consistent with the contrast shown in the bright-field TEM image (Fig. 2(e)), where the darker contract of nanoprecipitates are from weight contrast since Sn is much heavier than Si resulting in larger scattering to incident electron beam under TEM. Why these nanoprecipitates form is unclear and the exact mechanism behind this behavior require further investigation. One issue however pertinent: nanoprecipitates are much likely to be caused by the phase separation during melt spinning process.

The inset is the electron diffraction pattern of the nanocrystals where all the spots come from the cubic $Mg_2Si_{0.4}Sn_{0.6}$ crystal structure (JCPDS 01-089-4254), confirming that these nanocrystals and the matrix belongs to the cubic $Mg_2Si_{0.4}Sn_{0.6}$ phase. These nanoscaled precipitates have the characteristic length of 10-20 nm (the dark areas), which are completely invisible in the SEM images due to their truly fine structure. Figure 2(e) is the high-resolution TEM image of $Mg_{1.86}Li_{0.14}Si_{0.4}Sn_{0.6}$ showing the presence of nanocrystals. It is apparent that the nanoscaled particles have different crystal orientations when precipitated from the matrix, and the lattice spacing shows that these nanocrystals are the cubic $Mg_2Si_{0.4}Sn_{0.6}$ crystal structure. In addition, in order to verify that Li element is indeed incorporated in the compound of $Mg_2Si_{0.4}Sn_{0.6}$, EELS spectrum was taken to collect the Li–K edge. Figure 2(f) shows the EELS spectrum of the $Mg_{1.86}Li_{0.14}Si_{0.4}Sn_{0.6}$ , where the edge at 57 eV is identified as the Li-K edge and another peak edge can be identified as Mg-L [28-29]. This EELS spectrum strongly proved that Li-doped $Mg_2Si_{0.4}Sn_{0.6}$ samples were successfully synthesized.

The temperature dependences of electrical conductivity $\sigma$, Seebeck coefficient $S$ and power factor PF for $Mg_{2(1-x)}Li_{2x}Si_{0.4}Sn_{0.6}$ compounds between 300 and 773 K are displayed in Figure 3, while the Li content-dependent carrier concentration is shown in Figure 3(b). As shown in Figure 3(a), the undoped sample (x=0.00) exhibits typical intrinsic semiconductor behavior as electrical conductivity monotonically increases with increasing temperature; while all Li-doped samples show typical heavily doped degenerate semiconductor behavior as the electrical conductivity monotonically decreases with increasing temperature. In addition, electrical conductivity increases monotonously as the Li content increases. This observed enhancement of electrical conductivity in Li-doped samples is caused by the increase in carrier concentration upon Li doping. As shown in Figure 3(b), carrier concentration obviously increases with the increase of Li content.

Table 1 lists some physical properties of all samples at room temperature. The reduced Fermi level $\eta$ and Lorenz number $L$ are obtained from Eqs(1)–(4) by employing a single parabolic band (SPB) model under the relaxation time approximation and the electrical transport dominated by acoustic phonon scattering (r = -1/2) [22].

$$S = \pm \frac{K_B}{e}\left[ \eta_F - \frac{(r+5/2)\, F_{r+2/3}(\eta_F)}{(r+3/2)F_{r+1/2}(\eta_F)} \right] \quad (1)$$

$$F_i(\eta_F) = \int_0^\infty \frac{x^i dx}{1+\exp(x-\eta_F)} \quad (2)$$

$$\eta_F = E_F / (K_B T) \quad (3)$$

$$L = (\frac{K_B}{e})^2 \left\{ \frac{(r+7/2)F_{r+5/2}(\eta_F)}{(r+3/2)F_{r+1/2}(\eta_F)} - \left[ \frac{(r+5/2)F_{r+3/2}(\eta_F)}{(r+3/2)F_{r+1/2}(\eta_F)} \right]^2 \right\} \quad (4)$$

Where $\eta$, $F_i(\eta_F)$, $r$, and $K_B$ are the reduced Fermi energy, the Fermi integral, the scattering factor, and the Boltzmann constant, respectively. As shown in Table 1, Li is considered as an effective hole donor for $Mg_2Si_{0.4}Sn_{0.6}$compounds, which turns n-type semiconductor of $Mg_2Si_{0.4}Sn_{0.6}$ to p-type behavior and greatly enhances the holes concentration when Li doping increases. The holes concentrations of $Mg_{2(1-x)}Li_{2x}Si_{0.4}Sn_{0.6}$ samples at room temperature are $4.94\times10^{19}cm^{-3}$ and $2.35\times10^{20}cm^{-3}$ for x=0.01 and 0.09, respectively.

As one can see in Figure 3(c), the positive Seebeck coefficient indicates that the majority of charge carriers are holes. The absolute value of Seebeck coefficient decreases with the increase of Li-doping content at the same temperature. The values of Seebeck coefficient at room temperature are -390.1, 152.7, 112.3, 95.4, and 89.1μV/K for x=0, 0.01, 0.03, 0.07, 0.09, respectively. Obviously, such reduced Seebeck coefficient is due to the increase of carrier concentration upon Li doping. As we know, Seebeck coefficient $S \propto \frac{m^*}{(3n)^{2/3}}$ and carrier mobility $\mu = \frac{e\tau}{m^*}$, where $m^*$ is effective mass, $n$ is carrier concentration and $\tau$ is relaxation time. As shown in Table 1, the carrier mobility $\mu$ of these Li -doped samples decreases with the increase of Li doping, indicating that the effective mass is gradually increased. In addition, although the effective mass is enhanced upon Li doping, the Seebeck coefficient decreases. As such, the $S$ is principally influenced more by carrier concentration than the effective mass. The greatly enhanced electrical conductivity and slightly reduced Seebeck coefficient together lead to an improved power factor as plotted in Figure 3(d). Meanwhile, the sample with x=0.07 possesses the largest electrical conductivity as shown in Figure 3(a), leading to a highest power factor which reaches a maximum of 1.6 mW $K^{-2}m^{-1}$ at 760 K. This value is much higher than what has been reported in literatures on p-type $Mg_2(Si,Sn)$-based solid solutions [17,18,30].

The temperature dependence of thermal conductivity $k$, the lattice thermal conductivity $k_L$ including bipolar contribution $k_{Bi}$ and the dimensionless thermoelectric figure of merit ZT between 300 and 773 K are shown in Figure 4. We calculated the combined term ($k_L$+ $k_{Bi}$) by subtracting the electronic component $k_e$ from the total thermal conductivity $k$. The electronic conductivity $k_e = L\sigma T$ , where the Lorenz number $L$ have been calculated from Eqs(1)-(4) based on a single parabolic band model under the relaxation time approximation and assuming the dominance of acoustic phonon scattering [31-32]. In Figure 4(a), for all the samples, thermal conductivity $k$ decreases linearly with increasing temperature up to 500 K and shows an opposite trend due to the bipolar effect afterwards. In addition, for Li-doped samples, the thermal conductivity is higher than that of un-doped sample before the presence of bipolar effect. It can be inferred that the larger thermal conductivity of Li-doped samples is mainly ascribe to the monotonously enhanced electrical conductivity. However, upon the presence of bipolar effect, the thermal conductivity of Li-doped samples becomes lower than that of pure sample. It is worth mentioning that the thermal conductivity of all samples in our work is overall lower than that reported in literature [18], while the record ZT to date is obtained in our work in Li-doped p-type $Mg_2(Si,Sn)$-based materials. This result is because of the much finer microstructure and nanoscaled precipitates obtained by our melt-spinning processing as shown in our SEM and TEM results. As illustrated in Figure 4(b), below 500 K, the intrinsic excitation of carriers does not occur in the $Mg_{2(1-x)}Li_{2x}Si_{0.4}Sn_{0.6}$, thus the value of $k_L$+ $k_{Bi}$ mainly reflects the lattice part $k_L$. While at higher temperature, the lattice thermal conductivity $k_L$ is governed by Umklapp phonon scattering mechanism and approximately accord with the proportionality $k_L \propto 1/T$ [30,33]. Besides, it can be found that the onset of bipolar effect of $Mg_{2(1-x)}Li_{2x}Si_{0.4}Sn_{0.6}$ compounds shifted to higher temperature as the increasing amount of Li doping. This trend is reasonable based on the fact that the higher concentration of Li doping the larger the carrier density in $Mg_{2(1-x)}Li_{2x}Si_{0.4}Sn_{0.6}$ compounds.

In Figure 4(c), it is noted that the ZT values principally increase as the content of Li increases; while the peak of ZT is about 0.58 at around 760 K with x=0.07, around 15% higher than that reported in the literature [18]. Such

enhancement in ZT is mainly attributed to the improved power factor that benefits from the optimized carrier concentration and the lower thermal conductivity compared with literature data. Further improvement of ZT could be obtained by considering the following factors: (1) doping on the Sn or Si sites to further enhance point defect scattering and optimize the carrier density; (2) optimizing the melt spinning fabrication procedure to obtain much sharper and cleaner grains and grain boundaries in the final densified bulk, thereby further promoting charge transport; (3) preparing nanocomposite to largely decrease the thermal conductivity, in other words, dispersing metallic and/or non-metallic nanoparticles to our *p*-type $Mg_2(Si,Sn)$-based compounds, where various forms of nano-inclusions are uniformly dispersed. Meanwhile, one could broaden the range of embedded nanoparticle sizes to scatter phonons with much wider wavelength. All these scenarios seem very interesting and are being studied.

In this study, we successfully synthesized $Mg_{2(1-x)}Li_{2x}Si_{0.4}Sn_{0.6}$ compounds using the home-made melt spinning followed by spark plasma sintering method and investigated the effect of Li doping on electrical and thermal transport properties of p-type $Mg_{2(1-x)}Li_{2x}Si_{0.4}Sn_{0.6}$ compounds. It is found that Li doping rapidly elevates the hole carrier concentration, enhancing the electrical conductivity from $2.2 \times 10^3$ to $7.3 \times 10^4$ S/m along with decreased Seebeck coefficient to some extent. The thermal conductivity first increases upon Li doping till the presence of bipolar effect and then decrease. Furthermore, Li-doped samples exhibit significantly higher ZT than that of the undoped sample. The peak ZT reaches 0.58 around 760 K when x=0.07. Therefore, in this work, we have enhanced the thermoelectric properties on p-type $Mg_2(Si,Sn)$-based materials via Li doping, but their ZT are still much lower than that of n-type. Future effort is desired to enhance the thermoelectric performance of p-type $Mg_2(Si,Sn)$-based compounds so as to realize their commercialization of $Mg_2(Si,Sn)$-based thermoelectric devices for power generation application.

The work was financially supported in part by the National Natural Science Foundation of China (Grant no. 11344010, 11404044, 51472036, 51401202), the Fundamental Research Funds for the Central Universities (CQDXWL-2013-Z010).

This work at the Chongqing Institute of Green and Intelligent Technology, Chinese Academy of Sciences is supported by the One Hundred Person Project of the Chinese Academy of Science, Grant No. 2013-46.

[1] G.J. Snyder, E.S. Toberer, Nat. Mater. 7 (2008) 105–114.

[2] X. Y. Zhou, G. Y. Wang, L. Zhang, H. Chi, X. L. Su, J. Sakamoto, C. Uher, J. Mater. Chem. 22 (2012) 2958-2964.

[3] X. Zhang, L. D. Zhao, Journal of Materiomics. 1 (2015) 92-105.

[4] Y. G. Tang, Sinn-wen. Chen, G. Jeffrey Snyder, Journal of Materiomics. 1 (2015) 75-84.

[5] L.D. Zhao, V. P. Dravid, M. G. Kanatzidis, Energy Environmental. Science. 7 (2014) 251-268.

[6] X. Y. Zhou, G. W. Wang, L. J. Guo, H. Chi, G. Y. Wang, Q. F. Zhang, C.Q. Chen, T.Thompson, Jeff Sakamoto, V. P. Dravid, G. Z. Cao, C. Uher, J. Mater. Chem. A. 2 (2014) 20629-20635.

[7] K. Biswas, J. He, I. D. Blum, C.-I. Wu, T. P. Hogan, D. N. Seidman, V. P. Dravid, M. G. Kanatzidis. Nature. 489 (2012) 414.

[8] J. Tani, H. Kido, Journal of Alloys and Compounds. 466 (2008) 335–340.

[9] L. X. Chen, G. Y. Jiang, Y. Chen, Z. L. Du, X. B. Zhao, T. J. Zhu, J. He, J. Mater. Res. 26 (2011) 3038-3043.

[10] M. Søndergaard , M. Christensen ,K. A. Borup , H. Yin, B. B. Iversen, J Mater Sci. 48 (2013) 2002–2008.

[11] Z. L. Du, T. J. Zhu, Y. Chen, J. He, H. L. Gao, G. Y. Jiang, T. M. Tritt, X. B. Zhao, J. Mater. Chem. 22 (2012) 6838-6844.

[12] G.Y. Jiang, J. He, T.J. Zhu,C.G. Fu, X. H. Liu, L. P. Hu, X. B.Zhao, Adv. Funct. Mater. 24 (2014) 3776–3781.

[13] Q. Zhang, J. He, T.J. Zhu, S.N. Zhang, X.B. Zhao, T.M.Tritt, Appl. Phys. Lett. 93 (2008) 102-109.

[14] W. Liu, X. Tang, H. Li, K. Yin, J. Sharp, X. Zhou, C. Uher, J. Mater. Chem. 22 (2012) 13653–13661.

[15] P. Gao, X. Lu, Isil Berkun, Robert D. Schmidt, Eldon D. Case, Timothy P. Hogan, Appl. Phys. Lett. 105 (2014) 202104.

[16] H. Ihou-Mouko, C. Mercier, J. Tobola, G. Pont, H. Scherrer, J. Alloys Compd. 509 (2011) 6503–6508.

[17] Y. Isoda, S. Tada, T. Nagai, H. Fujiu, Y. Shinohara. J. Electron. Materials. 39 (2010) 1531–1535.

[18] Q. Zhang, L. Cheng, W. Liu, Y. Zheng, X. L. Su, H. Chi, H. J. Liu, Y.G. Yan, X.F. Tang, C. Uher, Phys. Chem. Chem. Phys. 16 (2014) 23576.

[19] W. Liu, Q. Zhang, K. Yin, H. Chi, X. Y. Zhou, X. F. Tang, C. Uher, Journal of Solid State Chemistry. 203 (2013) 333–339.

[20] H.Y. Chen, N. Savvides, Journal of Electronic Materials. 38 (2009) 1056-1060.

[21] L. Chuang, N. Savvides, T.T. Tan, S. Li. Journal of Electronic Materials. 39 (2010) 1971-1974.

[22] Q. Zhang, Y. Zheng, X. L. Su, K. Yin, X. F. Tang and C. Uher, Scripta Materialia. 96 (2015) 1–4.

[23] M. S. Dresselhaus, G. Chen, M. Y. Tang, R. G. Yang, H. Lee, D. Z. Wang, Z. F. Ren, J. P. Fleurial, P. Gogna. Adv. Mater. 19 (2007) 1043-1053.

[24] S. K. Bux, J. P. Fleurial, R. B. Kaner, Chem. Commun. 46 (2010) 8311-8324.

[25] L. Laughman, L.W. Davis, Solid State Communications. 9 (1971) 497—500.

[26] P. Bellanger, S. Gorsse, G. Bernard-Granger, C. Navone,A. Redjaimia, S. Vivès, Acta Materialia. 95 (2015) 102-110.

[27] X. Zhang, H. L.Liu, S. H. Li, F. P. Zhang, Q. M. Lu, J. X. Zhang, Materials Letters. 123 (2014) 31-34.

[28] C. Caha , O.L.Krivanek. EELS ATLAS. 1983.

[29] F. Cosandey, D. Su, M. Sina, N. Pereira, G.G. Amatucci, Micron. 43 (2012) 22-29.

[30] W. Liu, K. Yin, X. Su, H. Li, Y. Yan, X. Tang, C. Uher. Intermetallics. 32 (2013) 352–361.

[31] G. A. Slack, M. A. Hussain. J. Appl. Phys. 70 (1991) 2694-2781.

[32] Z. Du, T. Zhu, Y. Chen, J. He, H. Gao, G. Jiang, T. M. Tritt, X. Zhao. J. Mater. Chem. 22 (2012) 6838–6844.

[33] M. C. Roufosse, P. Klemens, J. Geophys. Res. 79 (1974) 703–705.

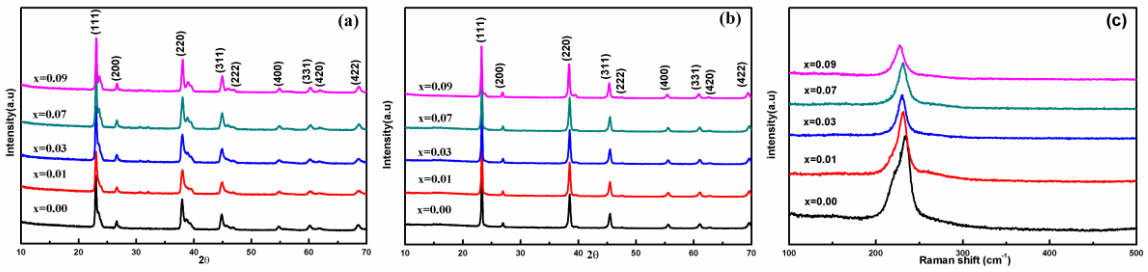


**Figure 1.** XRD patterns of $Mg_{2(1-x)}Li_{2x}Si_{0.4}Sn_{0.6}$ (x = 0.00, 0.01, 0.03, 0.07, 0.09) (a)ribbons after MS and (b) bulk after SPS.(c) Raman spectra of $Mg_{2(1-x)}Li_{2x}Si_{0.4}Sn_{0.6}$ sample

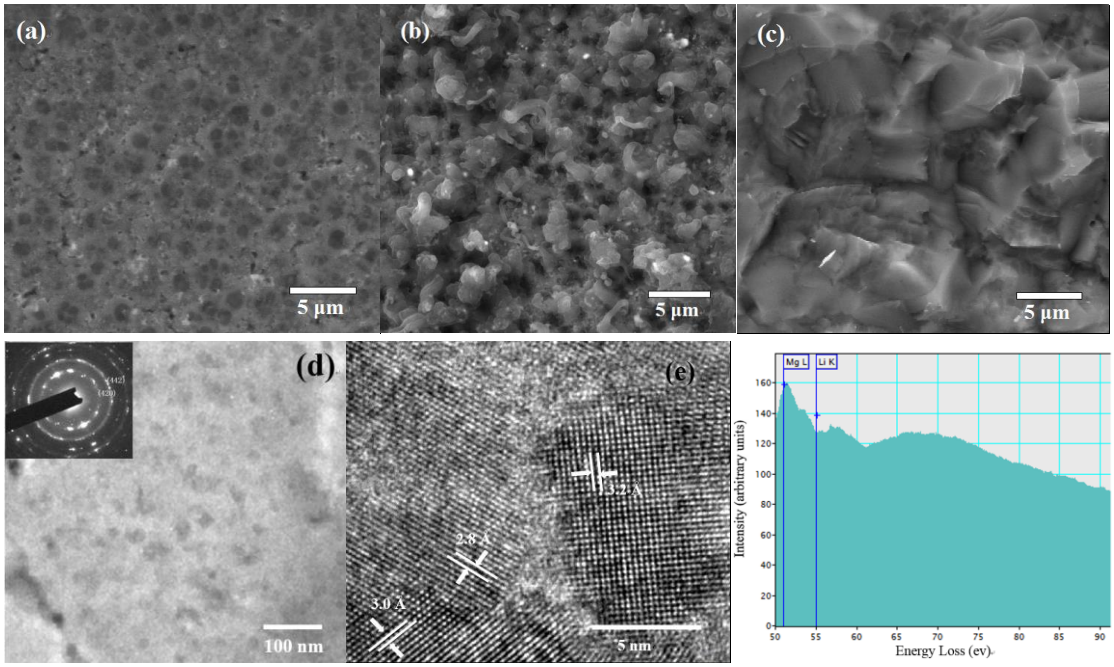


**Figure 2.** (a) Typical SEM of contact face; (b)free face of ribbons; (c) microstructure of fractured surfaces of synthesized bulk; (d) TEM image of the $Mg_{1.86}Li_{0.14}Si_{0.4}Sn_{0.6}$ and the inset is SAED pattern; (e) high resolution TEM image ; (f) Li–K edge taken from $Mg_{1.86}Li_{0.14}Si_{0.4}Sn_{0.6}$.

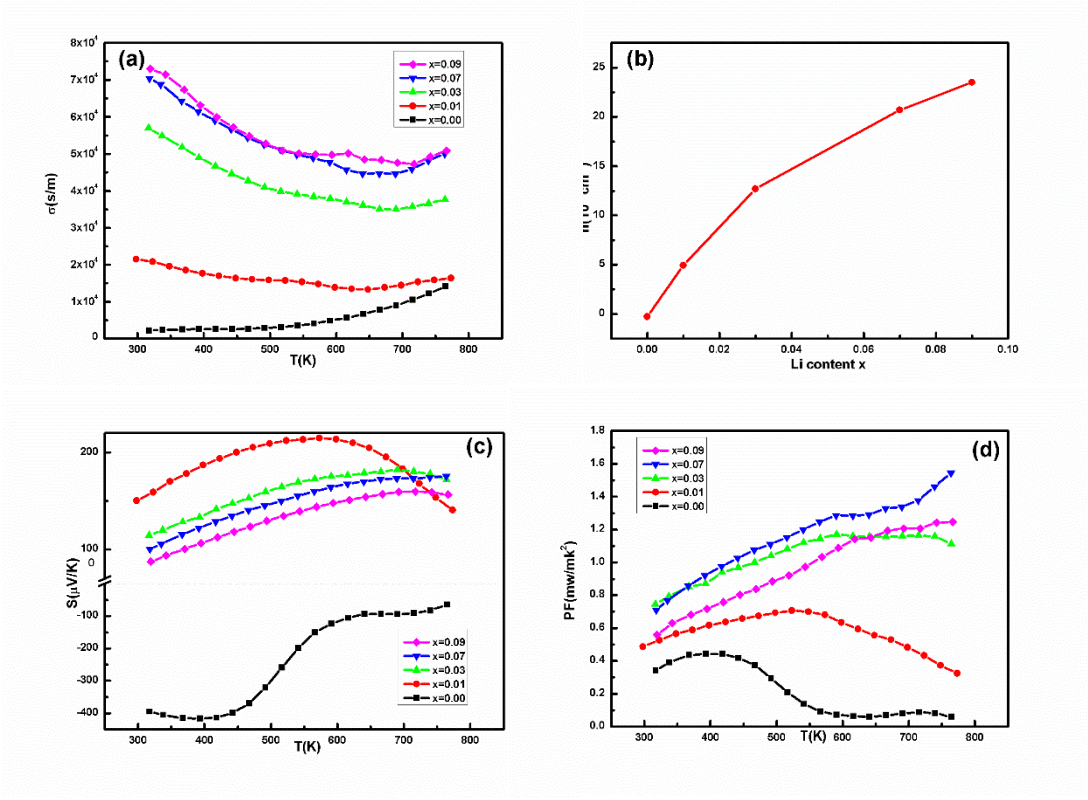


**Figure 3.** Temperature dependent electrical transport properties of $Mg_{2(1-x)}Li_{2x}Si_{0.4}Sn_{0.6}$ (x = 0.00, 0.01, 0.03, 0.07, 0.09). (a) Electrical conductivity; (b) Li content dependent carrier concentration; (c) Seebeck coefficient,(d) Power factor.

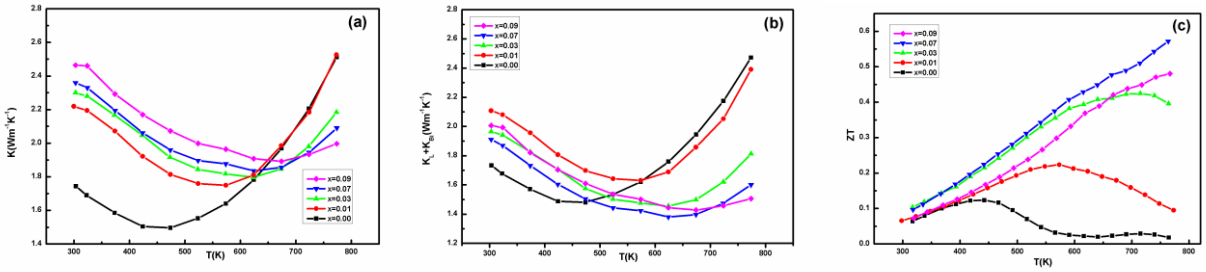


**Figure 4.** Temperature dependent thermal transport properties of $Mg_{2(1-x)}Li_{2x}Si_{0.4}Sn_{0.6}$ (x = 0.00, 0.01, 0.03, 0.07, 0.09). (a) thermal conductivity k , (b) combined lattice and bipolar thermal conductivities $k_L + k_{Bi}$, and (c) ZT values.